Khiem *et al.*
Sustainable Environment Research (2022) 32:48
https://doi.org/10.1186/s42834-022-00158-3

Sustainable Environment Research

RESEARCH

Open Access

Hollow and oval-configured ultrafine Co_3O_4 as a highly-efficient activator of monopersulfate for catalytic elimination of Azorubin S

Ta Cong Khiem[1], Duong Dinh Tuan[2], Eilhann Kwon[3], Bui Xuan Thanh[4], Yiu Fai Tsang[5], Venkata Subbaiah Munagapati[6], Jet-Chau Wen[6,7], Chechia Hu[8*] and Kun-Yi Andrew Lin[1,9*]

Abstract

Azorubin S (ARS) represents one of the most common and frequently-utilized toxic azo dyes produced from industrial activities. While various conventional treatment techniques could not effectively eliminate ARS from water, heterogeneous metal-based catalyst coupled with monopersulfate (MPS) is a highly-efficient process for eliminating ARS, in which tricobalt tetroxide (Co_3O_4) has been attracted increasing attention as a preeminent MPS activator due to its outstanding physicochemical properties. However, the nanoscale Co_3O_4 particles usually pose a limitation of serious agglomeration in the aqueous environment, thus lowering their efficiency. Thus, developing an easy-synthesized and exceptionally efficient Co_3O_4-based catalyst is crucially paramount. Therefore, in this work, a special hollow-structured oval-like cobalt oxide (abbreviated as HOCO) was successfully constructed using Co-metal organic framework as a precursor, which was then utilized for catalyzing activation of MPS to degrade ARS. This as-obtained HOCO exhibited distinct physicochemical characteristics from commercially-available Co_3O_4, which subsequently resulted in superior activities for MPS activation in ARS degradation. Specifically, 100% of ARS could be degraded in 30 min with a corresponding reaction kinetic of 0.22 min^{-1} by HOCO + MPS system. $SO_4^{\bullet-}$ radicals were validated to be primary reactive species for ARS degradation while the degradation pathway of ARS was also elucidated. This study further provides insightful information about the development of novel hollow-structured Co_3O_4-based catalyst for catalyzing activation of MPS to remove toxic dyes from water.

Keywords: Azorubin S, Monopersulfate, Hollow, Cobalt Oxide, Activation

1 Introduction

Nowadays, dyes are extensively employed as colorants and additives in foods, textiles, cosmetics, and pharmaceuticals [1]. It has been published that more than 10,000 types of dyes are available, in which azo dyes account for over half of the textile dyes employed in the industry [2]. Nevertheless, increasing release of these dye substances from wastewater effluents into water environments may lead to negative effects on ecology in view of their potential toxicities [3]. Among numerous types of dyes, azo dyes represent one of the largest categories [4]; however, most of azo dyes have been validated to exhibit toxicities, even carcinogenicity [5]. Specifically, Azorubin S (ARS), one of the most common red-colored dyes, has been consistently used in many products, but ARS has been considered as a carcinogenic and genotoxic compound [6]. While ARS has been banned in the United States, it is still available and consumed in many countries [7].

*Correspondence: chechia@mail.ntust.edu.tw; linky@nchu.edu.tw

[8] Department of Chemical Engineering, National Taiwan University of Science and Technology, Taipei City 106, Taiwan
[9] Innovation and Development Center of Sustainable Agriculture, National Chung Hsing University, Taichung 402, Taiwan
Full list of author information is available at the end of the article

Therefore, it is highly crucial to eliminate ARS from contaminated water.

Various techniques are already proposed for removing ARS from contaminated sources, such as adsorption [8], filtration [9], and biological treatments [10]. Unfortunately, these conventional techniques exhibit relatively low removal capabilities especially because of low bio-degradability of ARS [11]. Alternatively, advanced oxidation processes are advantageous techniques for eliminating refractory contaminants, and especially, sulfate-radical ($SO_4^{\bullet-}$)-type techniques are focused recently as sulfate radicals exhibit larger standard redox power, longer half-lives, and higher selectivity [12, 13]. For obtaining sulfate radicals, monopersulfate (MPS) has been increasingly utilized as MPS would be inexpensive and highly-accessible. Nonetheless, the auto-dissociation of MPS is extremely slow; therefore, MPS shall be activated for facilitating generation of sulfate radicals. To date, heterogeneous transition metal-based MPS activation is already validated to be the most practical technique to eliminate refractory organic pollutants [14]. For instance, Wang et al. synthesized a composite of iron, cobalt, and oxygen codoped g-C_3N_4 (Fe–Co–O–g-C_3N_4) for activating MPS to degrade sulfamethoxazole (SMX), and 100% of SMX was degraded in 30 min with a reaction rate of 0.085 min^{-1} [15]. Moreover, Lim's group prepared cobalt-doped black TiO_2 nanotubes to activate MPS for eliminating 4-chlorophenol (4-CP) in water, in which full 4-CP degradation was afforded within only 20 min with the corresponding degradation kinetic calculated as 0.28 min^{-1} [16]. This validates that heterogeneous transition metals would be advantageous for MPS activation. Therefore, the activation of MPS using heterogeneous metal-based catalysts should be also propitious to the elimination of ARS. Amid various transition metals, cobalt (Co)-based catalysts are preeminent MPS activators, in which tricobalt tetroxide (Co_3O_4) has attracted great attention owing to its outstanding physicochemical properties, redox capability and excellent reactivity [17, 18]. However, the nanoscale of Co_3O_4 particles usually pose a limitation of serious agglomeration in the aqueous environment [19–21], lowering their surface area, then diminishing the catalytic activity. Thus, the development of an exceptionally efficient Co_3O_4-based catalyst for MPS activation is crucial.

Lately, hollow-nanostructured materials (HNMs) represent a novel class of heterogeneous materials that have been focused and increasingly employed in different catalytic applications [22, 23]. The interesting characteristics of HNMs, such as large contact areas and pore volumes, abundant active sites, high permeability, and productive electron transfer capability make them useful materials for energy storage, catalysis, energy conversion, etc. [24]. More importantly, with the huge internal voids encapsulated by external thin shells, HNMs could offer maximum exposed active surfaces as well as minimize the agglomeration of nanoparticles (NPs) in the aqueous medium [25]. These outstanding features would be afforded by constructing a novel hollow-nanostructured Co_3O_4-based catalyst for MPS activation in water.

Herein, this work aims to prepare special a hollow-nanostructured Co_3O_4 with ultrafine Co_3O_4 NPs confined in an oval-like morphology using a Co-metal organic framework (MOF) as a precursor. Through one-step modification via a chemical-engraving step, then followed by calcination, Co-MOF was completely transformed into a hollow-nanostructured oval-like Co_3O_4, denoted as HOCO. This as-prepared HOCO was then employed for catalyzing MPS activation to eliminate ARS. Physicochemical properties of HOCO were thoroughly characterized, which were noticeably different with the conventional commercial Co_3O_4 NPs. Moreover, different influencing parameters, such as MPS dosage, catalyst dosage, temperatures, pH values, co-existing matters on ARS degradation would be also examined. Besides, the reactive oxygen species (ROS) involved in ARS degradation using HOCO-activated MPS were further determined. From the detected intermediate products and the density functional theory (DFT) calculation of ARS, a plausible degradation pathway of ARS was then revealed.

2 Experimental

2.1 Synthesis of HOCO and characterizations

In brief, Co-based MOF with an oval shape was synthesized by coordinating Co with the imidazolate ligand. The resulting Co-MOF was then chemically engraved to transform the oval Co-MOF to a hollow and oval cobaltic precursor, which was thermally oxidized in air to afford the hollow-structured oval Co_3O_4 (HOCO) as schemed in Fig. 1a. Initially, a Co-MOF with oval-like morphology was firstly prepared, followed by a modification step with tannimum via chemical-etching process before being calcined in air to obtain the final product. In a typical preparation, a solution containing 40 mL of Co $(NO_3)_2$ was slowly added into another solution bearing 40 mL of 2-methylimidazole (2-MIM) where the molar ratio of Co precursor to 2-MIM = 1:8. The mixture was then stirred vigorously at ambient temperature for 4 h. Subsequently, the resultant purple-colored precipitate was assembled via centrifugation, rinsed by deionized water, and dried at 65 °C overnight to afford oval-like Co-MOF. Next, a certain amount of the as-prepared oval-like Co-MOF (i.e., 200 mg) was then immersed into a solution containing 300 mL mixture of deionized water and ethyl alcohol (ratio = 1:1 in

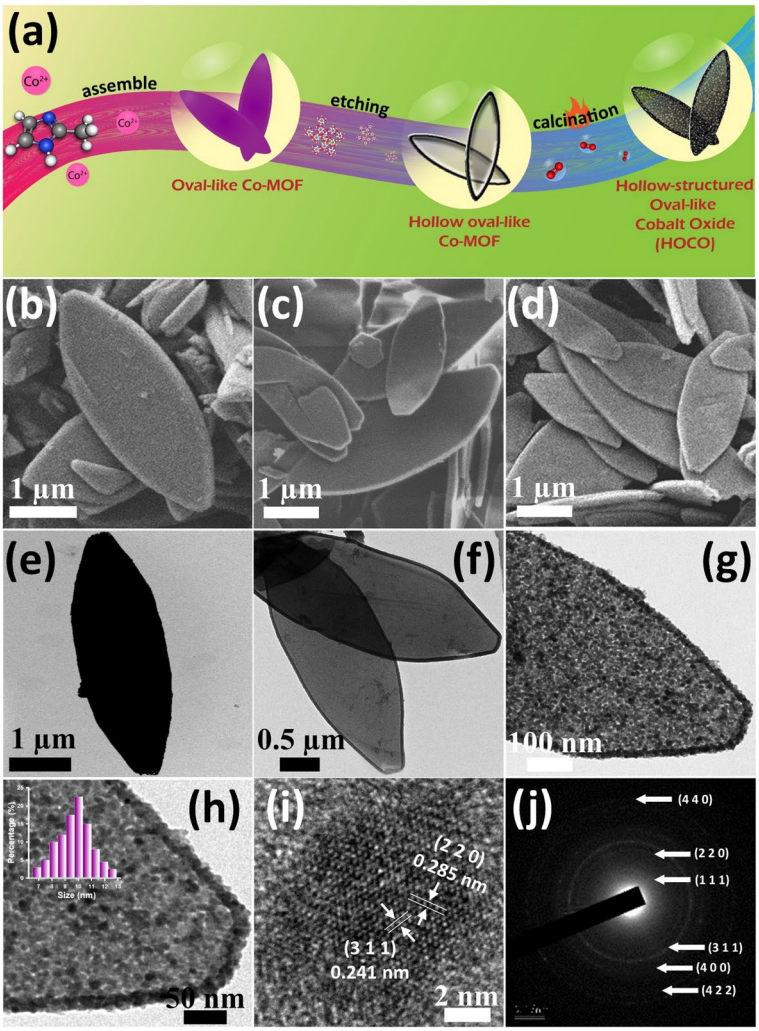

Fig. 1 (**a**) Flow-chart of HOCO preparation; (**b**) and (**e**) microscopic images of the original oval-like Co-MOF; (**c**) and (**f**) microscopic images of hollow oval-like Co-MOF; (**d**) and (**g**) SEM and TEM images of HOCO; (**h**) TEM image of HOCO at a closer magnification (the inset is the particle size distribution); (**i**) HRTEM image of HOCO; and (**j**) SAED of HOCO

volume) and tannimum (1 mg mL^{-1}) for 10 min to complete the chemical-etching process. The resulting product was then collected via centrifugation (8000 rpm), washed thoroughly by ethyl alcohol several times, and dried at 80 °C in a vacuum oven to acquire hollow oval-like Co-MOF. Finally, this as-prepared hollow oval-like Co-MOF was calcined in air at 600 °C for 4 h at a ramping rate of 2 °C min^{-1} to afford hollow-structured oval-like HOCO.

For material characterizations, the appearance of all materials was determined using Scanning Electron Microscope (SEM) and Transmission Electron Microscope (TEM) (JEOL JSM-7800F and JEM-1400, Japan). The elemental composition of HOCO was also analyzed using energy-dispersive X-ray spectroscopy (EDS) (Oxford Instruments, UK). Moreover, the crystalline structures of all as-prepared materials were characterized using an X-ray diffractometer, XRD (Bruker, USA). Besides, Raman spectroscopies of HOPO and commercial Co_3O_4 NP were verified using a Raman spectrometer (TII Nanofinder 30, Japan). The surface chemistry of HOCO was further examined using X-ray photoelectron spectroscopy (XPS) (ULVAC-PHI, PHI 5000, Japan). Additionally, the reducible behaviors of HOCO and commercial Co_3O_4 NP were further analyzed by H_2-temperature-programmed reduction (H_2-TPR) profiles using a chemisorption analyzer coupled with a *Thermal Conductivity D*etector (Anton Paar, ASIQ TPx, Austria). Next, the BET surface area and pore volume of HOCO were determined by N_2 sorption isotherms using a volumetric analyzer (Anton Paar Autosorb IQ, Austria).

The surface charges of HOCO were also verified using a Zetasizer (Nano-ZS, Malvern Instruments, UK).

2.2 Degradation of ARS

The degradation of ARS using HOCO-activated MPS was conducted using batch-type experiments. Typically, a certain amount of HOCO (i.e., 100 mg L^{-1}) was firstly added into ARS solution with the initial concentration (C_0) of ARS was 50 mg L^{-1} for 30 min to verify the adsorption of ARS. Next, 100 mg L^{-1} of MPS was instantly introduced to the ARS solution to start the degradation experiment. At a certain reaction time (t), sample aliquots (3 mL) were taken out and filtered to separate HOCO from the ARS solution. The remaining ARS concentration in the filtrate at t min (C_t) was subsequently determined by UV-Vis spectrophotometer with the absorption wavelength of 520 nm. For experimental sections, the effects of different parameters including different HOCO dosages, MPS dosages, various ARS concentrations, initial pH values, co-existing surfactants and salt, and inhibitors were investigated. The recyclability experiments were performed by collecting and re-employing the used HOCO. Moreover, for comparison, commercial Co_3O_4 NP (size 50 ~ 80 nm) was also used for MPS activation. ROS involving in the degradation of ARS by HOCO + MPS system were revealed by electron paramagnetic resonance (EPR) with a typical radical spin-trapping agent, namely 5,5-Dimethyl-1-pyrroline N-oxide (DMPO). The recyclability of HOCO for multiple ARS degradation cycles was also evaluated by re-using HOCO. Besides, the degradation intermediates produced from ARS degradation were further identified using a mass spectrometer (Thermo Finnigan, LCQ ion-trap mass spectrometer, USA). Total organic carbon (TOC) was analyzed using TOC analyzer (SHIMADZU TOC-5000, Japan).

3 Results and discussion

3.1 Properties of HOCO

First, morphologies of the as-prepared materials were visualized. Figure 1b and e present electronic microscopic figures of the original Co-MOF, indicating successful formation of 2-dimensional oval-like morphology. Its crystalline structure was also determined using XRD analysis as displayed in Fig. 2a, which is consistent with reported literature [26]. After this pristine Co-MOF was modified with tannium via a chemical-engraving process, the resultant product still retained the oval-like appearance of the original Co-MOF (Fig. 1c). However, it can be seen that the interior part of this product was removed, creating a huge hollow-structure inside whereas the thin outer layer (size ca. of 20-25 nm) was remained as shown in Fig. 1f, verifying the successful construction of hollow-structured oval-like Co-MOF. The XRD pattern of this product was also characterized as depicted in Fig. S1 of Supplemental Materials.

When this hollow-structured Co-MOF was thermally-oxidized in air, the resulting substance still showed the oval-like morphology and hollow configuration (Fig. 1c and g). Moreover, densely-packed and ultrafine spherical particles could be observed, which were distributed evenly throughout this calcined product (Fig. 1g); a closer observation in Fig. 1h then shows that the particles would be nano-sized, ranging from 7 to 13 nm (in diameter) with a principal size of 10 nm (Fig. 1h). Besides, its HRTEM (Fig. 1i) unveils two particular d-spacings of 0.29 and 0.24 nm, which corresponded to the plane (2 2 0) as well as (3 1 1) in Co_3O_4. This result validated that those nano-sized particles or NPs should be Co_3O_4, demonstrating the successful formation of hollow-structured oval-like cobalt oxide (HOCO).

The crystalline structure of HOCO was also measured (Fig. 2b); and its crystalline patterns exhibited several notable diffraction peaks located at 19, 31.4, 36.8, 38.6, 44.8, 55.5, 59.3, 65.1, 74.1 and 77.3°, which could be well indexed to those signature planes of Co_3O_4 (JCPDS #42-1467), asserting the full conversion of the oval-like cobaltic MOF to Co_3O_4. The electron diffraction pattern of HOCO in Fig. 1j reveals the polycrystalline structure of HOCO, which is correlated with its XRD profile. In addition, the elemental composition in HOCO was also identified using EDX analysis in Fig. S2a, where only Co and O could be noted. Besides, the elemental mapping of HOCO was also determined (Fig. S2b-d), showing that oxygen and cobalt were certainly present and uniformly distributed throughout the oval-like outer layer.

Moreover, the functional groups of the pristine oval-like Co-MOF and HOCO were determined through IR profiles (Fig. 2c). For the original Co-MOF, various absorption bands located at 500-1500 cm^{-1} shall be attributed to the ligand (i.e., an imidazole ring) [27]. Besides, an absorption band positioned at ~1584 cm^{-1} could be the C=N bond in 2-MIM, whereas two noticeable peaks located at 2929 and 3138 cm^{-1} could be corresponded to the C-H sp^3 in the aromatic ring and the C-H sp^2 in 2-MIM, respectively, further indicating the formation of Co-MOF [27]. The IR analysis of HOCO showed distinct absorption bands. Particularly, several notable bands detected in 565 and 660 cm^{-1} were attributed to Co^{2+} and Co^{3+} in cobalt oxide, respectively [28]. Besides, the bands located at 1630/3410 cm^{-1} were ascribed to the O-H bond, which was probably due to adsorbed H_2O on HOCO [29].

In addition, Raman spectroscopies of Co_3O_4 NP and HOCO were further characterized as shown in Fig. 2d. It can be noticed that both materials exhibited five

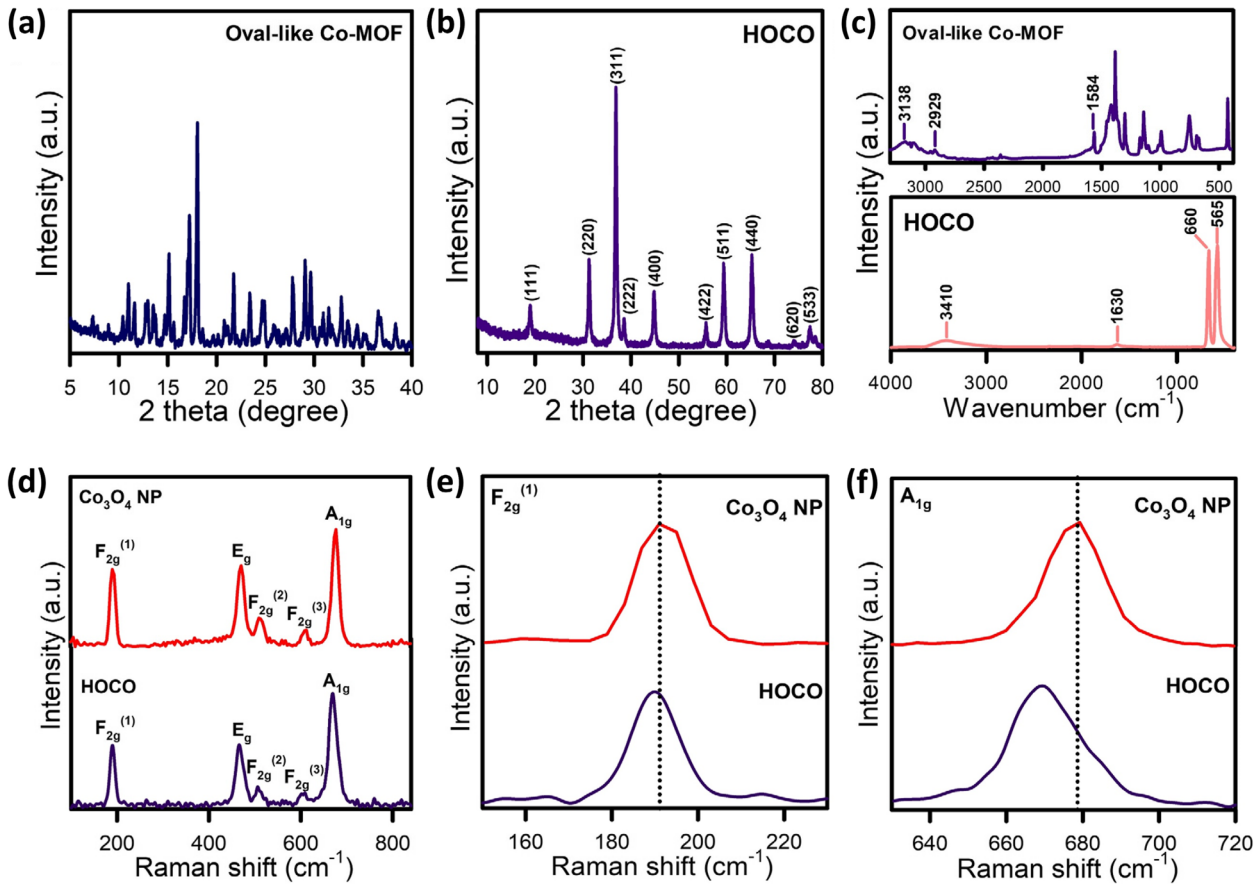

Fig. 2 (**a**) XRD pattern of the original oval-like cobaltic MOF; (**b**) XRD pattern of HOCO; (**c**) FTIR profiles of the pristine oval-like Co-MOF and HOCO; (**d**) long-range Raman spectroscopies of Co_3O_4 NP and HOCO; (**e**) and (**f**) Raman spectroscopies at specific regions

noticeable peaks, which could be assigned to the Raman active vibration modes (i.e., $A_{1g}+E_g+3F_{2g}$) of Co_3O_4 [30]. This further validates the formation of Co_3O_4 in HOCO. However, the peaks at $F_{2g}^{(1)}$ and A_{1g} regions of HOCO (Fig. 2e-f) were shifted to the lower positions than that of commercial Co_3O_4 NP. Specifically, the band at $F_{2g}^{(1)}$ region of HOCO was switched from 191 to 189 cm^{-1}, whereas the band at A_{1g} region was moved from 678 to 669 cm^{-1}. As these two specific regions were assigned to the oxygen mobility of Co_3O_4 [31], these shifted peaks in HOCO suggested that HOCO might possess more structural defects compared with Co_3O_4 NP, enabling HOCO to exhibit a more reactive surface [32], thereby enhancing activities of HOCO for MPS activation.

Furthermore, the chemical states of all elements in HOCO were identified by XPS. Figure 3a presents a whole-range scan, showing that only notable Co and O signals were detected, which was in line with EDX/mapping results. Besides, the Co2p spectra of HOCO were then deconvoluted into a number of peaks. The peaks detected in 779.4 and 794.3 eV were assigned to Co^{3+} species, whereas the peaks located at 781.4 and 796.5 eV were assigned to Co^{2+} species; and co-existence of these Co species strongly confirm the presence of Co_3O_4 in HOCO [33]. Moreover, the O1s spectra of HOCO was also examined, and a number of notable peaks were detected at 529.4 and 530.9 eV, derived from O species in metal-O bond (O_{latt}) and R-O bond (O_{ads}), respectively [34].

Additionally, since both commercial Co_3O_4 NP and HOCO were comprised Co_3O_4 and HOCO possessed more reactive surface, it was crucial to probe into the distinct reducibility between these two materials using H_2-TPR analysis. As displayed in Fig. 3d, H_2-TPR profiles of HOCO and Co_3O_4 NP are quite different, in which HOCO showed three reduction peaks and Co_3O_4 NP displayed two reduction bands. Typically, Co_3O_4 exhibits two reducing steps: the first step is the reducing step from Co^{3+} to Co^{2+} and the second step is the reducing step from Co^{2+} to Co^0 [35]. In the case of the commercial Co_3O_4 NP, these reduction bands were overlapped, in which the band at 465 °C was due to the first step, and

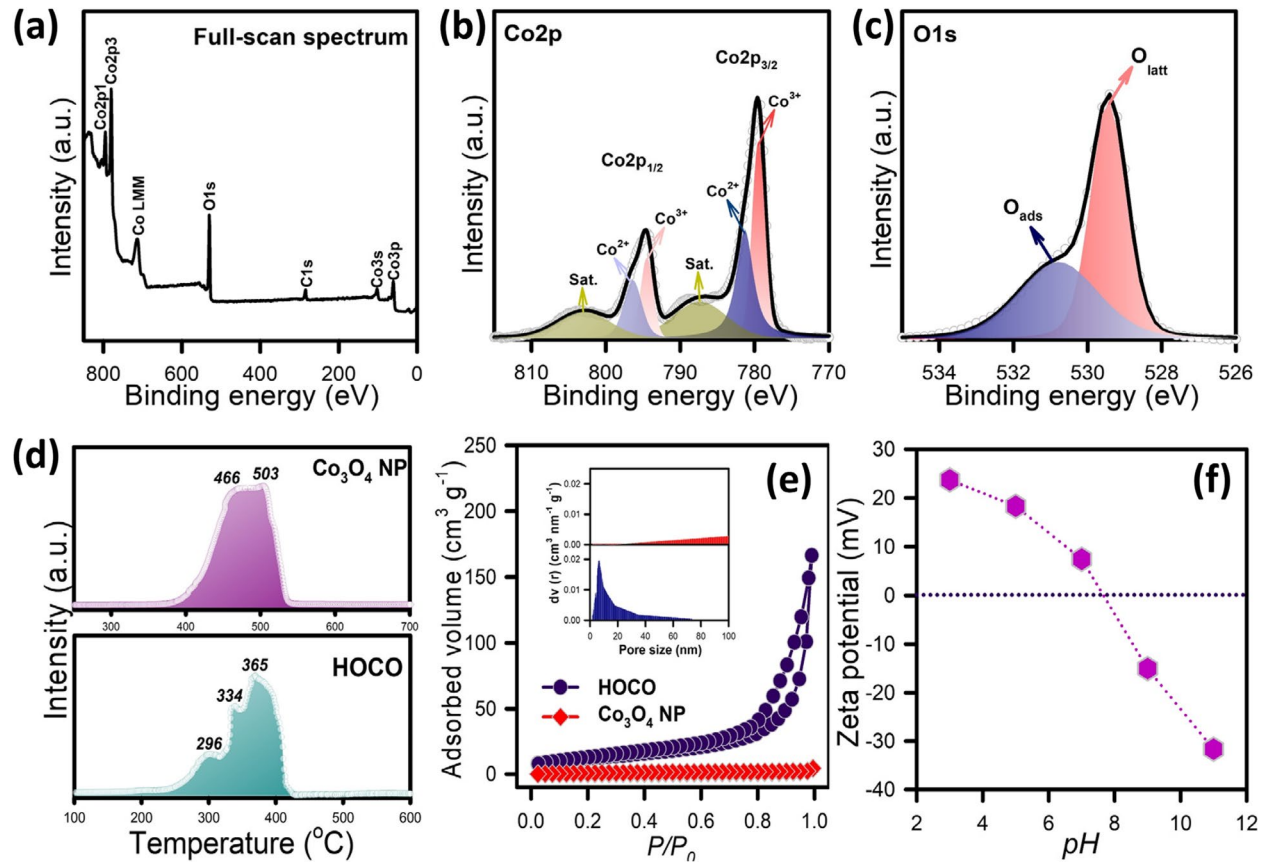

Fig. 3 XPS analysis of HOCO: (**a**) whole-range scan, (**b**) Co2p scan, and (**c**) O1s scan; (**d**) TPR analyses of Co_3O_4 NP and HOCO; (**e**) physical properties of Co_3O_4 NP and HOCO; and (**f**) zeta potential of HOCO at different pH values

the band at 501 °C was due to the second step. On the other hand, TPR analysis of HOCO showed three reductive bands at 296, 334, and 365 °C. Specifically, the peak at 296 °C could be due to the reducing step from Co^{3+} to Co^{2+} while these bands at 344 and 365 °C could correspond to the reducing step from Co^{2+} to Co^0 in the cluster form and bulk form, respectively [36]. This result showed that the reduction temperatures of Co species in HOCO were much lower than that of Co_3O_4 NP, further illustrating the higher degree of active surface in HOCO compared with Co_3O_4 NP, which subsequently contribute to different activities during oxidative reactions [37].

Next, the physical properties of both HOCO and Co_3O_4 NP were then characterized in Fig. 3e. HOCO exhibited an isotherm with hysteresis loop, suggesting mesopores contained in HOCO. The pore size analysis can be seen in the inset of Fig. 3e further validated the presence of mesopores and macropores in HOCO. The specific surface area of HOCO was then calculated as 44 $m^2 g^{-1}$ with a total porous volume = 0.26 $cm^3 g^{-1}$. On the other hand, the commercial Co_3O_4 NP showed a relatively low N_2 sorption capability; thus, its surface area would be merely 2.5 $m^2 g^{-1}$ with a certain small total porous volume of 0.001 $cm^3 g^{-1}$, probably due to the critical aggregation of these Co_3O_4 NPs as depicted in Fig. S3. This result further unveils the distinct textural properties between HOCO and Co_3O_4 NP, which would then influence their catalytic activities. These textural properties of HOCO and Co_3O_4 NP were also summarized in Table S1.

Moreover, since the degradation of ARS would be executed via batch-type degradation in water, zeta potentials of HOCO under numerous pH conditions were necessarily measured. Figure 3f shows the zeta potential profile of HOCO, illustrating that the zeta potentials of HOCO would be positive under acid and neutral conditions; and switched to negative charges at basic conditions. The zeta potential of HOCO would be 23.7 mV at pH = 3, and it would then decrease to 18.3 and 7.4 mV when pH increased to 5 and 7, respectively. When pH = 9, the zeta potential of HOCO would be − 15 mV, and it was further dropped to − 31.6 mV at pH = 11 with its pH_{zpc} = 7.6.

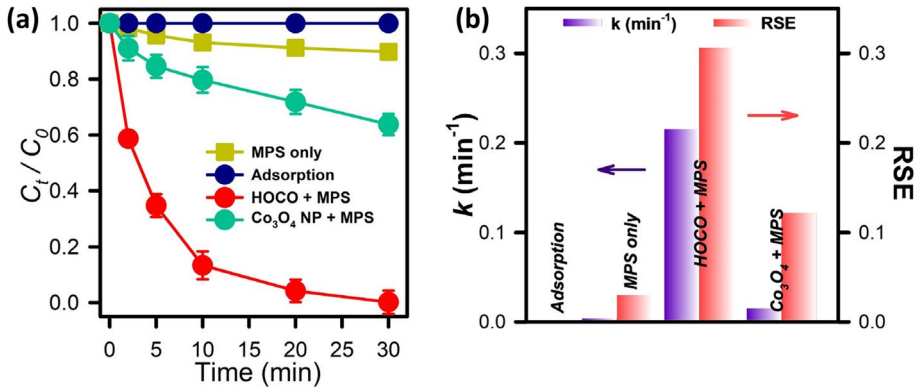

Fig. 4 (**a**) ARS elimination by various catalytic systems: MPS only, adsorption, Co_3O_4 NP + MPS, and HOCO + MPS; (**b**) the corresponding calculated degradation kinetics (*k*) (min^{-1}) and reaction stoichiometric efficiency (RSE) values of different catalytic systems on ARS degradation (Reaction conditions: catalyst = MPS:100 mg L^{-1}, T = 30 °C)

3.2 ARS degradation using HOCO-activated MPS

ARS degradation was investigated by different catalytic systems as shown in Fig. 4a. Initially, it was essential to test if ARS might be eliminated via the adsorption pathway. It can be noticed from Fig. 4a that ARS remained steady within 30 min with HOCO only, demonstrating the negligible adsorptive capability of ARS on HOCO surface. On the other hand, ARS was also hardly degraded in the presence of MPS individually since C_t/C_0 just approached 0.9, suggesting that MPS self-activation without catalysts would be ineffective, leading to low ARS degradation efficiency. Nevertheless, when HOCO was employed for MPS activation, ARS would be drastically reduced and wholly removed in 30 min. This result reveals that MPS could be activated by HOCO to result in ROS for degrading ARS. Moreover, as HOCO would be constituted of Co_3O_4, the commercial Co_3O_4 was also utilized for comparison with HOCO; and ca. 40% of ARS was eliminated after 30 min, proving that the commercial Co_3O_4 NP was also able to activate MPS for eliminating ARS. However, the ARS degradation efficiency by the commercial Co_3O_4 NP + MPS system was relatively low in comparison with that of HOCO + MPS system, indicating the benefit of HOCO for activating MPS to eliminate ARS. Besides, as ARS was efficiently degraded by HOCO coupled with MPS, the total organic carbon (TOC) should be then performed to determine the mineralization degree of ARS. The initial TOC (TOC_0) concentration was measured as 19 mg L^{-1}. As presented in Fig. S4, ca. 60% of TOC could be removed in 30 min, validating the decomposition of ARS using HOCO + MPS system.

On the other hand, for further comparing degradation efficiencies of ARS by the above-mentioned catalytic systems, two particular indices (i.e., degradation kinetics (*k*) (using the pseudo 1st order equation) [38] and reaction stoichiometric efficiency (RSE)) [39] were further calculated as the following equations (Eqs. (1)-(2)):

$$C_t = C_0 \exp(-kt) \tag{1}$$

$$RSE = \frac{ARS\ degraded\ (mol)}{Amount\ of\ MPS\ used\ (mol)} \tag{2}$$

where *k* denotes the pseudo 1st-order reaction rate. In Fig. 4b, the corresponding *k* of HOCO + MPS was calculated as 0.22 min^{-1}, which would be substantially higher than that of Co_3O_4 NP + MPS (0.015 min^{-1}), MPS individually (0.0036 min^{-1}) and adsorption (0.0017 min^{-1}). The as-calculated *k* of HOCO + MPS is much higher than other reported *k* values for ARS degradation in literature, such as 0.06 min^{-1} (FeCF + PC) [40], 0.035 min^{-1} (Fc + SPC) [41], and 0.089 min^{-1} (CoCNF + Ox) [42]. Besides, HOCO + MPS exhibited the highest RSE value of 0.31, followed by Co_3O_4 NP + MPS (0.12), MPS individually (0.03) and adsorption (0.001). Moreover, to shed a light on the advantage of this unique characteristic, we also prepared non-hollow structure oval-like Co_3O_4 NPs (abbreviated as SOCO) followed the same procedure for preparing HOCO, except the chemical-engraving process and employed it for ARS degradation. As depicted in Fig. S5, ca. 80% of ARS was removed when SOCO was coupled with MPS, showing that though SOCO was also capable to activate MPS to degrade ARS, the catalytic activity of SOCO without hollow-structured property was assuredly lower than that of HOCO. This further validated the excellent activity of HOCO to activate MPS, enabling it to be an effective heterogeneous activator for degrading ARS.

3.3 Effects of HOCO and MPS dosages, and different ARS concentrations

Since ARS was effectively degraded using HOCO-activated MPS, the effects of HOCO dosages and MPS dosages should play critical roles in ARS degradation. Thus, different amounts of HOCO and MPS were then investigated to examine their influence for obtaining the optimal condition for further investigations. As shown in Fig. 5a, ARS degradation efficiency would be improved by the increase of HOCO concentrations. Particularly, at 50 mg L^{-1} of HOCO, ARS gradually degraded as C_t/C_0 approached 0.05 in 30 min, and its corresponding k would be 0.095 min^{-1} (the inset of Fig. 5a). As the dosage of HOCO was raised to 100 mg L^{-1}, ARS would be completely eliminated in 30 min, and it would be reached in an even less reaction time (i.e., 20 min) at 150 mg L^{-1} of HOCO. The calculated k would be also measured as 0.22 min^{-1} as well as 0.34 min^{-1} at the HOCO dosage of 100 and 150 mg L^{-1}, respectively. This verifies the advantage of higher HOCO concentrations on ARS degradation, owing to the contribution of abundant active sites for accelerating ROS generated from MPS activation.

In addition, the influence of MPS concentrations on ARS degradation was also studied as illustrated in Fig. 5b. As a small dosage of MPS (i.e., 50 mg L^{-1}) was added, only 60% of ARS was eliminated in 30 min, probably because of insufficient ROS generated. Once MPS concentration was augmented to 100 mg L^{-1}, complete ARS degradation would be achieved in 30 min. A higher MPS dosage at 150 mg L^{-1} slightly enhanced the ARS degradation efficiency (Fig. 5b). This result revealed that the lower dosage of MPS with deficient generated ROS could not fully eliminate ARS while higher MPS dosages could effectively and completely remove ARS owing to sufficient ROS produced. Besides, the corresponding k with various MPS dosage would be also measured inside Fig. 5b. The corresponding k value at 50 mg L^{-1} of MPS was computed to be 0.095 min^{-1}, and it was then substantially raised to 0.22 as well as 0.27 min^{-1} at MPS dosage of 100 and 150 mg L^{-1}, which further validated the enhancing effect of relatively high MPS concentrations on ARS degradation.

Furthermore, it was practical for evaluating the activity of HOCO for catalyzing activation of MPS to eliminate different ARS concentrations. In Fig. 5c, the full

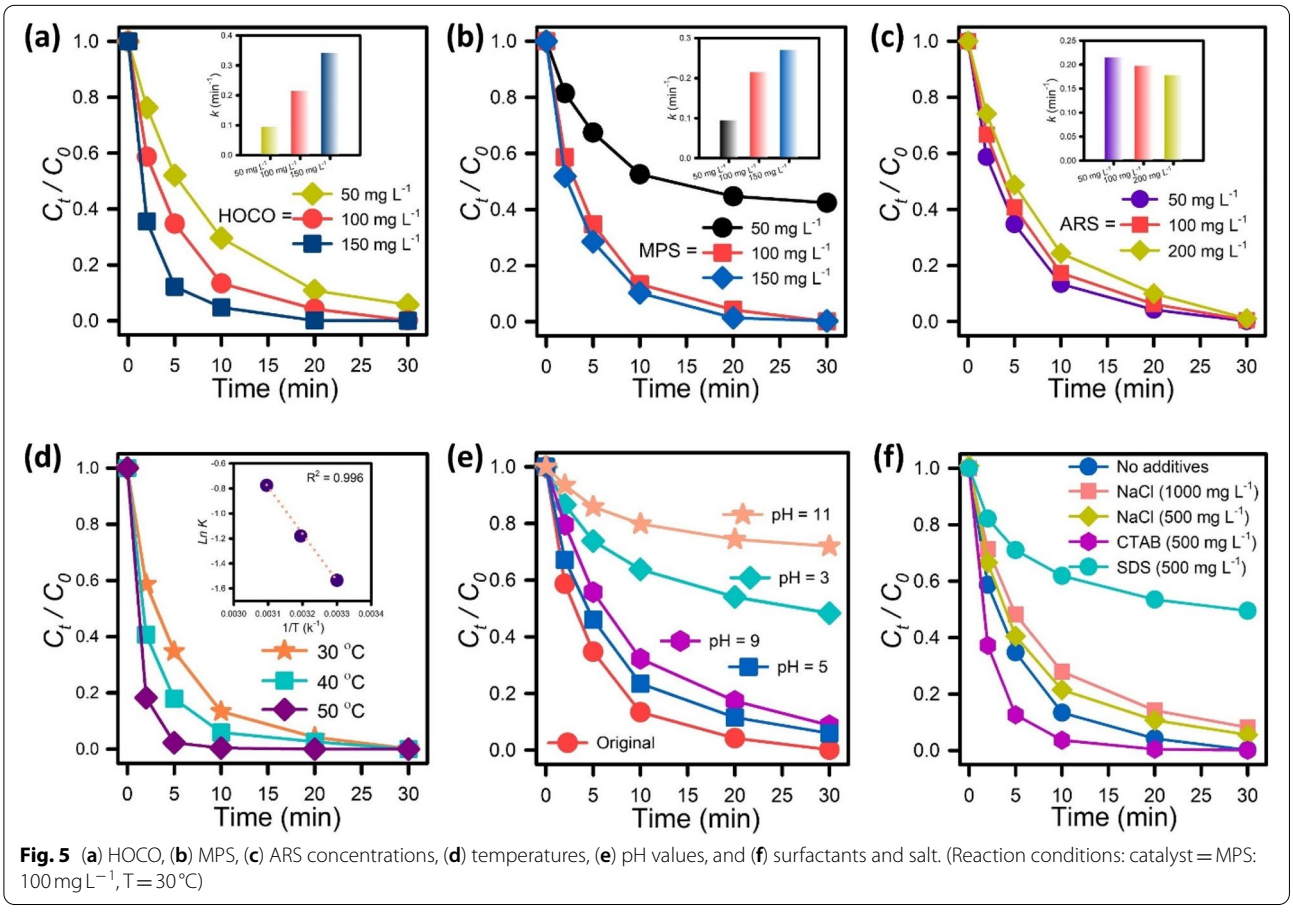

Fig. 5 (**a**) HOCO, (**b**) MPS, (**c**) ARS concentrations, (**d**) temperatures, (**e**) pH values, and (**f**) surfactants and salt. (Reaction conditions: catalyst = MPS: 100 mg L^{-1}, T = 30 °C)

degradation of ARS was still afforded in 30 min, even in a high-concentrated ARS solution (200 mg L^{-1}), confirming a superior performance of HOCO for activating MPS. In addition, the *k* values (Fig. 5c) were measured to be 0.22, 0.20, and 0.19 min^{-1} at the ARS concentration of 50, 100, and 200 mg L^{-1}, respectively. This further indicates that HOCO could retain its exceptional performance for MPS activation to eliminate ARS at various concentrations.

3.4 Influences of other factors

As ARS was efficiently degraded using HOCO-catalyzed MPS, the effects of other parameters on ARS elimination should be further investigated. First, the effect of temperatures was examined because temperatures are essential in the reaction kinetic (Fig. 5d). Generally, the degradation efficiency of ARS would be significantly boosted when temperature increases. Particularly, at 30 °C (Fig. S6a), the complete degradation of ARS was afforded within 30 min with its corresponding *k* of 0.22 min^{-1}. When the temperature raised to 40 and 50 °C, ARS degradation efficiencies were significantly enhanced as C_t/C_0 reached zero within shorter reaction times. And the corresponding *k* values were also drastically increased to 0.31 as well as 0.46 min^{-1} at 40 and 50 °C. This result assuredly proves the promoting effect of elevated temperatures on ARS elimination using HOCO-activated MPS.

Moreover, as the corresponding *k* raised with increasing temperatures, the relationship between *k* and *T* would be further correlated via the following equation (Eq. (3)) [43]:

$$\ln k = -\frac{E_a}{RT} + \ln A \tag{3}$$

where E_a represents the calculated activation energy (kJ mol^{-1}). The inset of Fig. 5d further shows the relationship between *k* and temperatures was fitted linearly with $R^2 = 0.996$. Thus, the activation energy (E_a) was then computed as 31 kJ mol^{-1}. This calculated E_a value from HOCO-activated MPS was comparatively lower than most reported E_a values in literature (Table S2), further validating the exceptional catalytic activity of HOCO, enabling it a highly-competitive catalyst for MPS activation.

The influence of different initial pH values on ARS degradation was then investigated. Figure 5e shows that ARS was completely degraded in 30 min at a neutral condition of pH = 7 with *k* of 0.22 min^{-1} (Fig. S6b). When the pH in ARS solution would be tuned to pH = 5, a weakly acidic environment, ARS degradation was slightly interfered as C_t/C_0 approached 0.1 after 30 min. The interference became more pronounced once pH was further tuned to a strongly acidic environment (i.e., pH = 3) since merely 50% of ARS was eliminated, and the corresponding degradation kinetic was significantly reduced to 0.024 min^{-1}. ARS degradation using HOCO-activated MPS was thus unfavorable in the acidic environment, which possibly due to the fact that MPS was indolent under acidic conditions [44], thereby suppressing MPS activation. Besides, the generated ROS (e.g., $SO_4^{\bullet-}$, $^{\bullet}OH$) might be quickly consumed by free protons as follows (Eqs. (4)-(5)) [45], lowering the degradation of ARS.

$$H^+ + {}^{\cdot}OH + e^- \rightarrow H_2O \tag{4}$$

$$H^+ + SO_4^{\cdot-} + e^- \rightarrow HSO_4 \tag{5}$$

Moreover, as pKa of ARS is 6.5 [46], ARS might be relatively positive due to the protonation. According to the zeta potentials of HOCO, its surface charge seemed to become relatively positive at pH < 6.5. Thus, the repulsion between the protonated ARS, and HOCO grew stronger, constraining their reactions [47]. Furthermore, H^+ might react with free radicals at low pH [48], thus suppressing ARS degradation, and hydrogen bonding of O-O and H^+ on MPS itself in acidic environments would limit reactions MPS with HOCO [49].

Additionally, the degradation efficiency of ARS would be also affected at higher pH. Particularly, under a weak basic condition of pH = 9, ARS degradation would be minimally influenced as C_t/C_0 still reached 0.15 in 30 min (Fig. 5e), and its corresponding *k* was 0.094 min^{-1}. Nevertheless, as pH changed to 11, a strongly basic environment, only 30% of ARS was removed whereas the degradation kinetic at pH = 11 was noticeably decreased to 0.011 min^{-1}. The negative impact of basic environment on ARS degradation, which would be possibly correlated to the much more intensive electrostatic repulsion between the relatively anionic surface of HOCO and SO_5^{2-} as pH exceeded the pKa of MPS = 9.4, then constricting the production of ROS [20]. Moreover, in the basic conditions, $SO_4^{\bullet-}$ radicals would readily react with excessive OH^- ions to become $^{\bullet}OH$ radicals which possess a shorter half-life and lower standard redox potential, leading to fewer $SO_4^{\bullet-}$ radicals involved in ARS degradation [20]. Moreover, in the basic conditions, $SO_4^{\bullet-}$ radicals would readily react with excessive OH^- ions (Eq. (6)) to become $^{\bullet}OH$ radicals which possess a shorter half-life and lower standard redox potential [50], leading to fewer $SO_4^{\bullet-}$ radicals involved in ARS degradation.

$$SO_4^{\cdot-} + OH^- \rightarrow SO_4^{2-} + {}^{\cdot}OH \tag{6}$$

On the other hand, in actual water systems, various compounds (including natural and artificial substances) are frequently detected, which potentially interfere

ARS elimination using HOCO-activated MPS. Therefore, it was important to scrutinize the effect of these compounds on ARS elimination (Fig. 5f). The effect of inorganic salt was first examined. In this study, sodium chloride (NaCl) at different concentrations was particularly selected as an inorganic salt model. With 500 mg L^{-1} of NaCl, ARS was still effectively degraded since almost 100% ARS was achieved in 30 min whereas ARS elimination was negligibly influenced at a higher concentration of NaCl (i.e., 1000 mg L^{-1}), suggesting the minimal interference of NaCl on ARS degradation using HOCO + MPS. This could be explained that the resultant $SO_4^{\bullet-}$ radicals would interact with free Cl^- ions to produce chloride radicals as following equations (Eqs. (7)-(8)) [51] that possess a relatively low redox power than that of $SO_4^{\bullet-}$ radicals, thereby diminishing ARS degradation efficiencies. Nonetheless, HOCO-activated MPS system still efficiently eliminated ARS, even at a higher NaCl concentration, validating that HOCO could retain its preeminent catalytic activity for MPS activation. The corresponding k with NaCl was also calculated as shown in Fig. S6c.

$$SO_4^{\cdot-} + Cl^- \rightarrow SO_4^{2-} + Cl^{\cdot} \quad (7)$$

$$Cl^{\cdot} + Cl^- \rightarrow Cl_2^{\cdot-} \quad (8)$$

Moreover, it was also reported that the existence of surfactants may also interfere the activation of MPS, decreasing the degradation effectiveness of the organic pollutants. Thus, it is useful to determine the influence of surfactants in water on ARS elimination using HOCO + MPS. Specific surfactants were chosen, including cetyltrimethylammonium bromide (CTAB) and sodium dodecyl sulfate (SDS) as shown in Fig. 5f. In the case of CTAB, it is interesting that ARS elimination was improved since C_t/C_0 approached zero in a shorter reaction time with k of 0.23 min^{-1} (Fig. S6c). This reveals positive influences of CTAB to ARS degradation by HOCO-catalyzed MPS, which was probably because CTAB, a typical cationic surfactant, may occupy HOCO surface, resulting in attraction between positively-charged HOCO surface and ARS molecules where ROS were produced [42], thus noticeably enhancing the degradation of ARS. With SDS (500 mg L^{-1}), a typical anionic surfactant, ARS degradation efficiency was certainly influenced since solely ca. 50% of ARS was eliminated in 30 min with a much lower k of 0.023 min^{-1}. The degradation of ARS using HOCO + MPS was much less effective in the co-existence of SDS, which was possibly because the surface of HOCO became negatively after SDS was introduced, creating a stronger electrostatic repulsion between negatively-charged HOCO surface and ARS molecules, then restricting the degradation of ARS [42].

3.5 Recyclability of HOCO

Since HOCO could effectively activate MPS to degrade ARS in water, it would be more intriguing to examine the reusability of HOCO for multiple ARS degradation cycles. It can be noticed from Fig. 6a that almost 100% of ARS was still afforded over 5 degradation cycles, indicating that HOCO could retain its exceptional performance for continuous activation of MPS. Besides, the crystalline pattern of the spent HOCO (Fig. 6b) was consistent with the pristine HOCO, showing that the highly-crystalline structure of HOCO was still retained. This indicated the outstanding durability of HOCO, enabling it to be a useful catalyst for MPS activation to eliminate ARS in water.

3.6 Identification of ROS involved in ARS degradation

In order to reveal the generation of potential ROS (e.g., $SO_4^{\bullet-}$, $^{\bullet}OH$) from HOCO-activated MPS as the following equations (Eqs. (9)-(11)) [52, 53], and their contribution to the degradation of ARS, the scavenging test by two specific radical scavengers, such as methyl alcohol (MeOH) and *tert*-butyl alcohol (TBA), was performed.

$$Co^{2+}@HOCO + HSO_5^- \rightarrow Co^{3+}@HOCO + SO_4^{\cdot-} + OH^- \quad (9)$$

$$Co^{3+}@HOCO + HSO_5^- \rightarrow Co^{2+}@HOCO + SO_5^{\cdot-}OH^- \quad (10)$$

$$SO_4^{\cdot-} + H_2O \rightarrow SO_4^{2-} + {}^{\cdot}OH + H^+ \quad (11)$$

Figure 6c shows that ARS elimination was inhibited by either MeOH or TBA. It can be noted that TBA comprises no α-hydrogen in its structure, TBA would promptly react with $^{\bullet}OH$; thus, it was selected to be an $^{\bullet}OH$ quencher. Figure 6c reveals that only 65% of ARS was degraded in 30 min by TBA with k decreased to 0.036 min^{-1} (Fig. S6d), demonstrating the existence of $^{\bullet}OH$ produced during the activation of MPS.

With α-hydrogen in the structure, MeOH can react with both $^{\bullet}OH$ and $SO_4^{\bullet-}$. The inhibitory effect became even more remarkable when MeOH was then added as C_t/C_0 merely reached 0.98, and k was significantly dropped to 0.0005 min^{-1}, implying that $SO_4^{\bullet-}$ was also generated from HOCO + MPS system. To confirm these ROS, EPR was further adopted using DMPO as a radical trapping probe. From Fig. 6d, it can be observed that there was no obvious pattern when MPS was individually

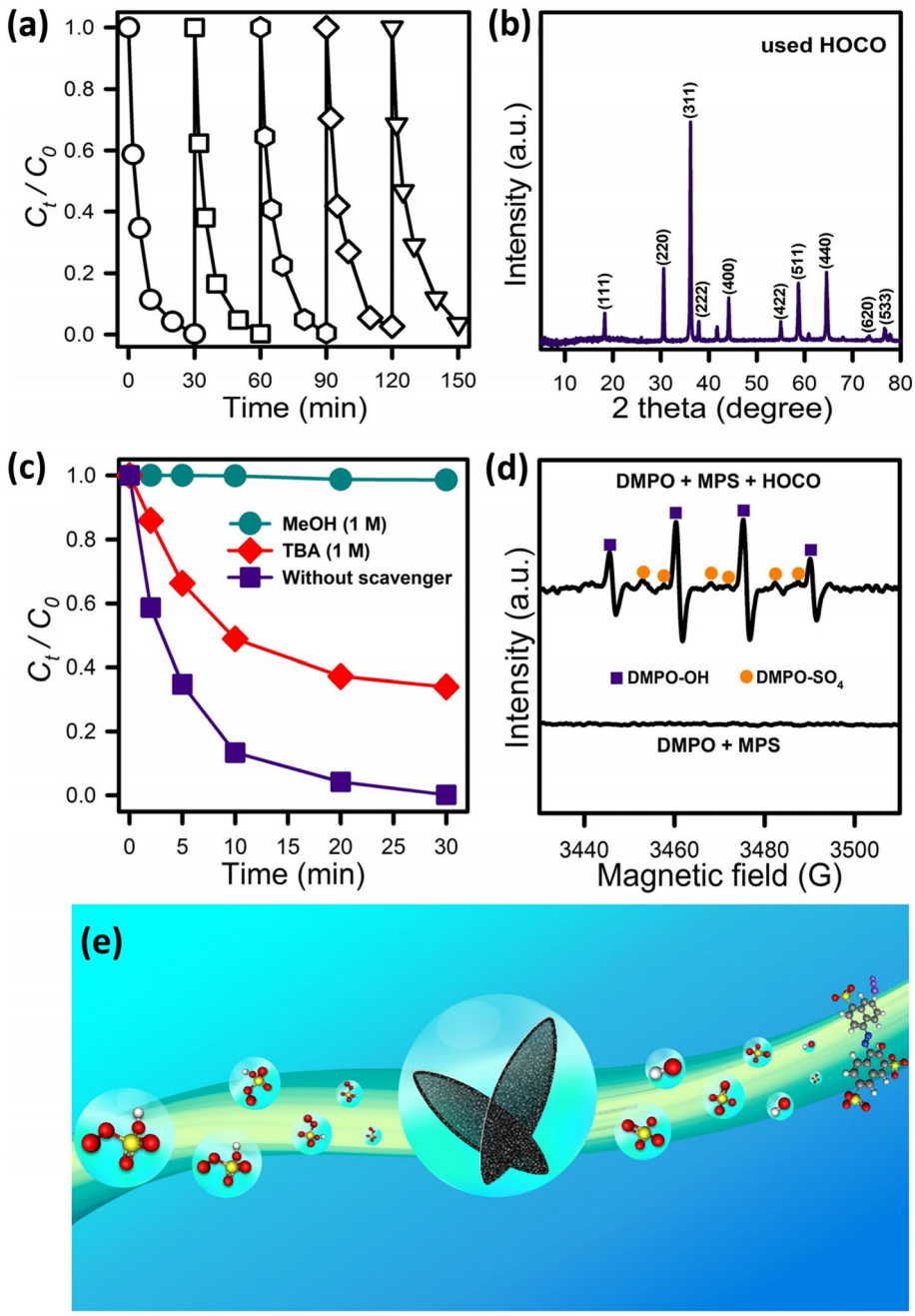

Fig. 6 (**a**) recyclability of HOCO over multiple ARS degradation cycles; (**b**) XRD pattern of the used HOCO; (**c**) influence of radical scavengers on ARS elimination using HOCO + MPS; (**d**) EPR analysis. (Reaction conditions: HOCO = MPS: 100 mg L^{-1}, T = 30 °C)

introduced in DMPO solution. Nevertheless, once HOCO and MPS were simultaneously added, notable patterns were particularly detected, which was attributed to DMPO-OH and DMPO-SO_4 adducts [54, 55]. This further proves the generation of $SO_4^{\bullet-}$ and $^{\bullet}OH$ species involved in ARS degradation using HOCO + MPS system (as shown Fig. 6e).

3.7 A potential degradation process for ARS

For elucidating ARS elimination process, computational calculations of ARS molecule according to the DFT were executed. Detailed computational settings were described in SI, and the geometrically-optimized ARS were then revealed in Fig. 7a by atom labels. Moreover, the highest occupied and lowest unoccupied

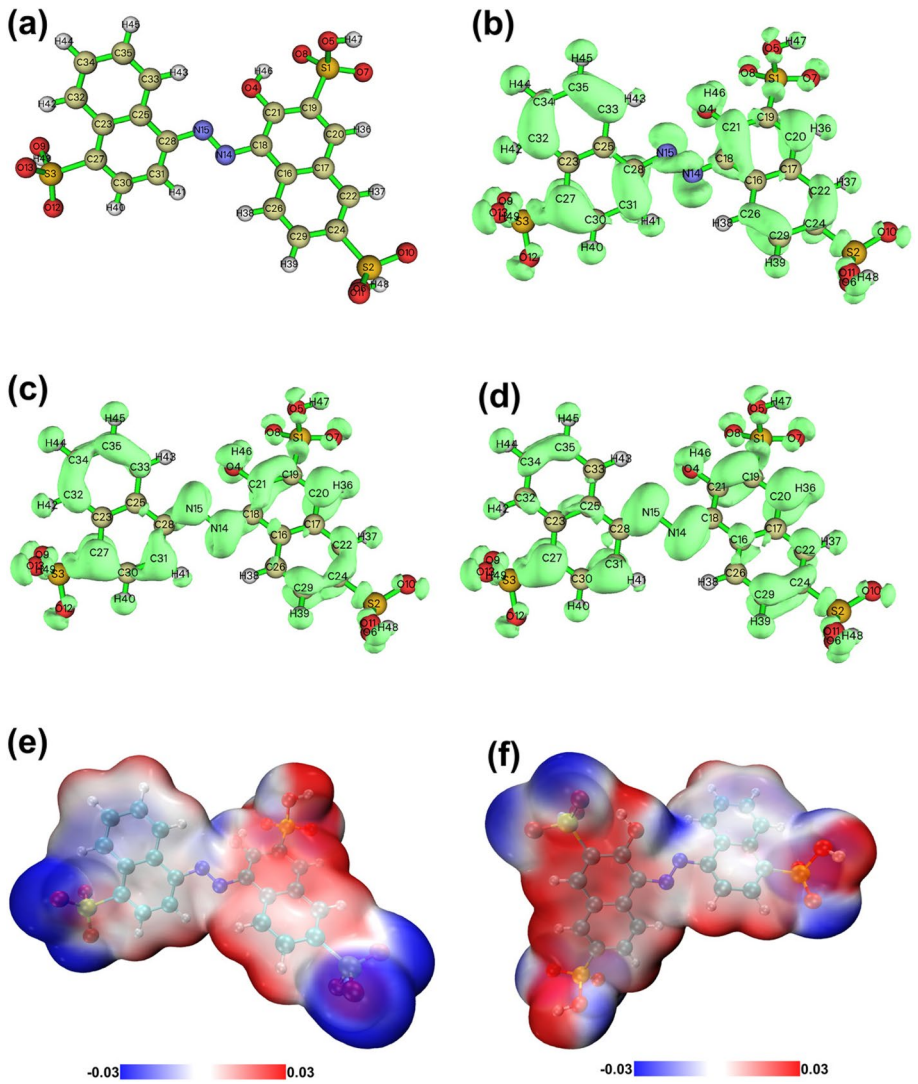

Fig. 7 Mapped isosurface of Fukui function of ARS: (**a**) labels of atoms, (**b**) f^-, (**c**) f^0, and (**d**) f^+, (**e**) the front-view, and (**f**) back-view ESP-mapped surface of ARS

molecular orbitals (MOs) of the geometrically-optimized ARS are also rendered in Fig. S7. Specifically, red and green-colored isosurfaces of these MOs represent electron-abundant and electron-deficient zones, respectively. Moreover, the highest occupied MO located on the naphthalene group bound to the sulfonate group tended to denote electrons. Therefore, ARS would possibly attract electrophilic attacks by the electrophilic ROS.

For further examining the degradation pathway by identifying the most-likely reaction spots of ARS, the Fukui function was adopted to provide insights [56]. To this end, the dual descriptor of the Fukui function was calculated, and rendered by Multiwfn to forecast potential reaction spots of ARS [57]. For offereing intuitive visualization of reactive spots of ARS, its corresponding isosurface of electron density derived from the Fukui function is then depicted, and Fig. 7b, c, and d display the f^-, f^0 and f^+ isosurfaces of ARS, respectively.

Theoretically, a spot with a huger green-colored isosurface would imply a higher possibility for reactions. Therefore, the electrophilic reaction spots of ARS (e.g., C27, C32, C33, N14, N15, etc.) would withdraw attacks by electrophilic radicals. Besides, Fig. 7c also displays possible spots for non-radical reactions, including C27, N14, and N15. These aforementioned spots might withdraw attacks to initiate the degradation process of ARS. On the other hand, the electrostatic potential (ESP)

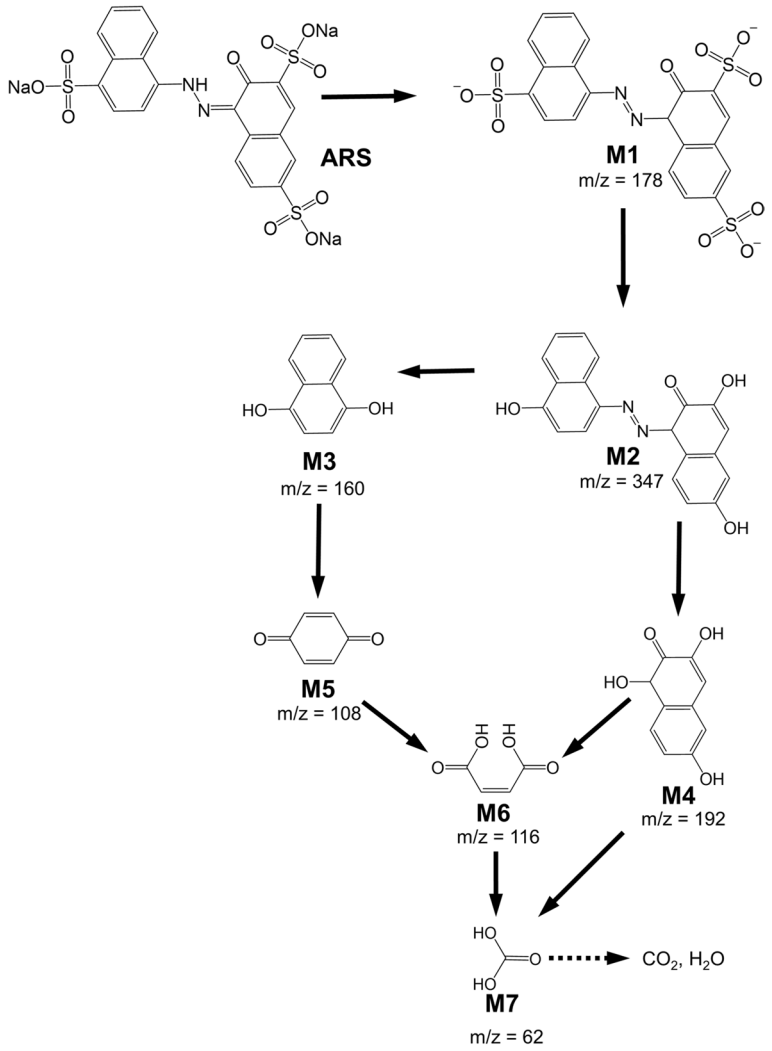

Fig. 8 A potential degradation pathway of ARS by HOCO-activated MPS

of ARS (Fig. 7e-f) also indicates that C19, C24, and C27 might exhibit affinities towards the anionic sulfate radical.

To clarifying the degradation process of ARS, degradation derivations from ARS were then determined in Fig. S8 with probable intermediates then outlined (Table S3). According to these intermediates, a probable ARS elimination process using HOCO is illustrated in Fig. 8 [58, 59]. In the beginning, ARS would be transformed to M1 upon dissolving in water, which was then attacked by the electrophilic ROS on those sites adjacent to the sulfonate group to afford an intermediate, M2. Through the cleavage of *N*=N bond, M2 would be then decomposed to produce M3, and M4. M3 was then further oxidized, and decomposed to generate M5, whereas M4 would be oxidized to result in M6 as well as M7 afterwards. On the other hand, M5 would be continuously oxidized to M6, and then M7, which was eventually decomposed to CO_2 and H_2O.

4 Conclusions

In brief, this study has successfully reported a special Co_3O_4-based catalyst using an oval-like Co-MOF as a precursor. Through a modification step with tannimum via the chemical-engraving process**,** hollow-structured oval-like Co-MOF was achieved, which was then calcined in air to become hollow oval-like cobalt oxide (HOCO). This HOCO was then adopted for catalyzing MPS activation to eliminate ARS. From material characterization results, HOCO exhibited highly-reactive surfaces and larger structures than commercial Co_3O_4 NP, contributing to the preeminent

catalytic activity of HOCO for MPS activation to eliminate ARS in water. Moreover, HOCO-activated MPS also showed relatively low activation energy (E_a) of 31 kJ mol^{-1}, which was substantially lower than many reported studies in the literature. Besides, HOCO would also preserve its activities over multiple degradation cycles without any significant loss as well as remaining its highly-crystalline structure. These results certainly confirm that HOCO could be an efficient heterogeneous activator for activating MPS to remove a toxic azo dye, ARS, in water.

Supplementary Information

The online version contains supplementary material available at https://doi.org/10.1186/s42834-022-00158-3.

Additional file 1.

Acknowledgements
This work is supported by the Ministry of Science and Technology (MOST) (111-2636-E-005-003-), Taiwan. The authors gratefully acknowledge the use of SQUID000200 of MOST111-2731-M-006-001 belonging to the Core Facility Center of National Cheng Kung University.

Authors' contributions
Ta Cong Khiem and Duong Dinh Tuan contribute to this study equally. Ta Cong Khiem prepared the draft, Duong Dinh Tuan curated data and prepared the draft, Eilhann Kwon curated data, Bui Xuan Thanh curated data and prepared visualization, Yiu Fai Tsang curated data and investigated, Venkata Subbaiah Munagapati edited the draft, Jet-Chau Wen reviewed the draft, Chechia Hu wrote and edited the draft, Kun-Yi Andrew Lin designed and analyzed experiments. All authors read and approved the final manuscript.

Funding
This work is supported by the Ministry of Science and Technology (MOST) (111-2636-E-005-003-), Taiwan.

Availability of data and materials
All data generated or analyzed during this study are provided.

Declarations

Competing interests
The authors declare they have no competing interests.

Author details
[1]Department of Environmental Engineering, National Chung Hsing University, Taichung 402, Taiwan. [2]International School, Thai Nguyen University, Thai Nguyen 250000, Viet Nam. [3]Department of Earth Resources and Environmental Engineering, Hanyang University, Seoul 222, South Korea. [4]Faculty of Environment and Natural Resources, Ho Chi Minh City University of Technology, Ho Chi Minh City 700000, Viet Nam. [5]Department of Science and Environmental Studies, The Education University of Hong Kong, New Territories, Hong Kong. [6]Research Center for Soil & Water Resources and Natural Disaster Prevention, National Yunlin University of Science and Technology, Douliu 640, Taiwan. [7]Department of Safety, Health, and Environmental Engineering, National Yunlin University of Science and Technology, Douliu 640, Taiwan. [8]Department of Chemical Engineering, National Taiwan University of Science and Technology, Taipei City 106, Taiwan. [9]Innovation and Development Center of Sustainable Agriculture, National Chung Hsing University, Taichung 402, Taiwan.

Received: 13 June 2022 Accepted: 19 October 2022
Published online: 05 December 2022

References

1. Ong SA, Min OM, Ho LN, Wong YS. Comparative study on photocatalytic degradation of mono azo dye Acid Orange 7 and Methyl Orange under solar light irradiation. Water Air Soil Poll. 2012;223:5483–93.
2. Daneshvar N, Rabbani M, Modirshahla N, Behnajady MA. Photooxidative degradation of Acid Red 27 in a tubular continuous-flow photoreactor: influence of operational parameters and mineralization products. J Hazard Mater. 2005;118:155–60.
3. Forgacs E, Cserhati T, Oros G. Removal of synthetic dyes from wastewaters: a review. Environ Int. 2004;30:953–71.
4. Benkhaya S, M'rabet S, El Harfi A. Classifications, properties, recent synthesis and applications of azo dyes. Heliyon. 2020;6:e03271.
5. Gicevic A, Hindija L, Karacic A. Toxicity of azo dyes in pharmaceutical industry. In: Badnjevic A, Skrbic R, Gurbeta Pokvic L, editors. CMBEBIH 2019. Proceedings of the International Conference on Medical and Biological Engineering. Cham: Springer; 2020. p. 581–7.
6. Sarikaya R, Selvi M, Erkoc F. Evaluation of potential genotoxicity of five food dyes using the somatic mutation and recombination test. Chemosphere. 2012;88:974–9.
7. Barros WRP, Steter JR, Lanza MRV, Motheo AJ. Degradation of amaranth dye in alkaline medium by ultrasonic cavitation coupled with electrochemical oxidation using a boron-doped diamond anode. Electrochim Acta. 2014;143:180–7.
8. Devi LG, Kumar SG. Exploring the critical dependence of adsorption of various dyes on the degradation rate using Ln^{3+}-TiO_2 surface under UV/solar light. Appl Surf Sci. 2012;261:137–46.
9. Rosu MC, Socaci C, Floare-Avram V, Borodi G, Pogacean F, Coros M, et al. Photocatalytic performance of graphene/TiO_2-Ag composites on amaranth dye degradation. Mater Chem Phys. 2016;179:232–41.
10. Ghodake G, Jadhav U, Tamboli D, Kagalkar A, Govindwar S. Decolorization of textile dyes and degradation of mono-azo dye amaranth by *Acinetobacter calcoaceticus* NCIM 2890. Indian J Microbiol. 2011;51:501–8.
11. Carvalho JRS, Amaral FM, Florencio L, Kato MT, Delforno TP, Gavazza S. Microaerated UASB reactor treating textile wastewater: The core microbiome and removal of azo dye Direct Black 22. Chemosphere. 2020;242:125157.
12. Wang SZ, Wang JL. Synergistic effect of PMS activation by Fe-^{0}@Fe_3O_4 anchored on N, S, O co-doped carbon composite for degradation of sulfamethoxazole. Chem Eng J. 2022;427:131960.
13. Chen X, Zhou J, Yang HW, Wang H, Li HX, Wu SJ, et al. PMS activation by magnetic cobalt-N-doped carbon composite for ultra-efficient degradation of refractory organic pollutant: mechanisms and identification of intermediates. Chemosphere. 2022;287:132074.
14. Kohantorabi M, Moussavi G, Giannakis S. A review of the innovations in metal- and carbon-based catalysts explored for heterogeneous peroxymonosulfate (PMS) activation, with focus on radical vs. non-radical degradation pathways of organic contaminants. Chem Eng J. 2021;411:127957.
15. Wang SZ, Liu Y, Wang JL. Peroxymonosulfate Activation by Fe-Co-O-codoped graphite carbon nitride for degradation of sulfamethoxazole. Environ Sci Technol. 2020;54:10361–9.
16. Lim J, Yang Y, Hoffmann MR. Activation of Peroxymonosulfate by oxygen vacancies-enriched cobalt-doped Black TiO_2 nanotubes for the removal of organic pollutants. Environ Sci Technol. 2019;53:6972–80.
17. Li P, Lin YN, Zhao S, Fu Y, Li WQ, Chen R, et al. Defect-engineered Co_3O_4 with porous multishelled hollow architecture enables boosted advanced oxidation processes. Appl Catal B-Environ. 2021;298:120596.
18. Xie RJ, Ji J, Huang HB, Lei DX, Fang RM, Shu YJ, et al. Heterogeneous activation of peroxymonosulfate over monodispersed Co_3O_4/activated carbon for efficient degradation of gaseous toluene. Chem Eng J. 2018;341:383–91.
19. Deng J, Feng SF, Zhang KJ, Li J, Wang HY, Zhang TQ, et al. Heterogeneous activation of peroxymonosulfate using ordered mesoporous Co_3O_4 for the degradation of chloramphenicol at neutral pH. Chem Eng J. 2017;308:505–15.
20. Guo WL, Su SN, Yi CL, Ma ZM. Degradation of antibiotics amoxicillin by Co_3O_4-catalyzed peroxymonosulfate system. Environ Prog Sustain. 2013;32:193–7.
21. Chen XY, Chen JW, Qiao XL, Wang DG, Cai XY. Performance of nano-Co_3O_4/peroxymonosulfate system: kinetics and mechanism study using Acid Orange 7 as a model compound. Appl Catal B-Environ. 2008;80:116–21.

22. Zeng T, Zhang XL, Wang SH, Niu HY, Cai YQ. Spatial confinement of a Co_3O_4 catalyst in hollow metal-organic frameworks as a nanoreactor for improved degradation of organic pollutants. Environ Sci Technol. 2015;49:2350–7.
23. Lu ZW, Dang Y, Dai CL, Zhang Y, Zou P, Du HJ, et al. Hollow MnFeO oxide derived from MOF@MOF with multiple enzyme-like activities for multi-function colorimetric assay of biomolecules and Hg^{2+}. J Hazard Mater. 2021;403:123979.
24. Hu WH, Zheng MB, Xu BY, Wei Y, Zhu W, Li Q, et al. Design of hollow carbon-based materials derived from metal-organic frameworks for electrocatalysis and electrochemical energy storage. J Mater Chem A. 2021;9:3880–917.
25. Huang Y, Fang YJ, Lu XF, Luan DY, Lou XW. Co_3O_4 hollow nanoparticles embedded in mesoporous walls of carbon nanoboxes for efficient lithium storage. Angew Chem Int Edit. 2020;59:19914–8.
26. Cai C, Zhang H, Zhong X, Hou LW. Ultrasound enhanced heterogeneous activation of peroxymonosulfate by a bimetallic Fe-Co/SBA-15 catalyst for the degradation of Orange II in water. J Hazard Mater. 2015;283:70–9.
27. Geng PB, Cao S, Guo XT, Ding JW, Zhang ST, Zheng MB, et al. Polypyrrole coated hollow metal-organic framework composites for lithium-sulfur batteries. J Mater Chem A. 2019;7:19465–70.
28. Herrero M, Benito P, Labajos FM, Rives V. Nanosize cobalt oxide-containing catalysts obtained through microwave-assisted methods. Catal Today. 2007;128:129–37.
29. Hu H, Cai SX, Li HR, Huang L, Shi LY, Zhang DS. In situ DRIFTs investigation of the low-temperature reaction mechanism over Mn-doped Co_3O_4 for the selective catalytic reduction of NO_x with NH_3. J Phys Chem C. 2015;119:22924–33.
30. Wang YZ, Wei XH, Hu XB, Zhou W, Zhao YX. Effect of formic acid treatment on the structure and catalytic activity of Co_3O_4 for N_2O decomposition. Catal Lett. 2019;149:1026–36.
31. Diallo A, Beye AC, Doyle TB, Park E, Maaza M. Green synthesis of Co_3O_4 nanoparticles via *Aspalathus linearis*: physical properties. Green Chem Lett. Rev 2015;8:30–6.
32. Wang Z, Wang WZ, Zhang L, Jiang D. Surface oxygen vacancies on Co_3O_4 mediated catalytic formaldehyde oxidation at room temperature. Catal Sci Technol. 2016;6:3845–53.
33. Wei RJ, Fang M, Dong GF, Lan CY, Shu L, Zhang H, et al. High-index faceted porous Co_3O_4 nanosheets with oxygen vacancies for highly efficient water oxidation. ACS Appl Mater Inter. 2018;10:7079–86.
34. Zhang L, He WH, Xiang X, Li Y, Li F. Roughening of windmill-shaped spinel Co_3O_4 microcrystals grown on a flexible metal substrate by a facile surface treatment to enhance their performance in the oxidation of water. RSC Adv. 2014;4:43357–65.
35. Tang CW, Wang CB, Chien SH. Characterization of cobalt oxides studied by FT-IR, Raman, TPR and TG-MS. Thermochim Acta. 2008;473:68–73.
36. Zheng YF, Yu YQ, Zhou H, Huang WZ, Pu ZY. Combustion of lean methane over Co_3O_4 catalysts prepared with different cobalt precursors. RSC Adv. 2020;10:4490–8.
37. Gong D, Zeng GF. Low-temperature combustion of methane over graphene templated Co_3O_4 defective-nanoplates. Sci Rep-UK. 2021;11:12604.
38. Wang QF, Shao YS, Gao NY, Chu WH, Chen JX, Lu X, et al. Activation of peroxymonosulfate by Al_2O_3-based $CoFe_2O_4$ for the degradation of sulfachloropyridazine sodium: kinetics and mechanism. Sep Purif Technol. 2017;189:176–85.
39. Khan MAN, Klu PK, Wang CH, Zhang WX, Luo R, Zhang M, et al. Metal-organic framework-derived hollow Co_3O_4/carbon as efficient catalyst for peroxymonosulfate activation. Chem Eng J. 2019;363:234–46.
40. Hsiao CY, Hung C, Kwon E, Huang CW, Huang CF, Lin KYA. Electrospun nanoscale iron oxide-decorated carbon fiber as an efficient heterogeneous catalyst for activating percarbonate to degrade Azorubin S in water. J Water Process Eng. 2021;40:101838.
41. Lin KYA, Lin JT, Lin YF. Heterogeneous catalytic activation of percarbonate by ferrocene for degradation of toxic amaranth dye in water. J Taiwan Inst Chem E. 2017;78:144–9.
42. Lin KYA, Lin JT, Lu XY, Hung C, Lin YF. Electrospun magnetic cobalt-embedded carbon nanofiber as a heterogeneous catalyst for activation of oxone for degradation of Amaranth dye. J Colloid Interf Sci. 2017;505:728–35.
43. Tuan DD, Chang FC, Chen PY, Kwon E, You SM, Tong SP, et al. Covalent organic polymer derived carbon nanocapsule-supported cobalt as a catalyst for activating monopersulfate to degrade salicylic acid. J Environ Chem Eng. 2021;9:105377.
44. Tan CQ, Gao NY, Deng Y, Deng J, Zhou SQ, Li J, et al. Radical induced degradation of acetaminophen with Fe_3O_4 magnetic nanoparticles as heterogeneous activator of peroxymonosulfate. J Hazard Mater. 2014;276:452–60.
45. Lai LD, Yan JF, Li J, Lai B. Co/Al_2O_3-EPM as peroxymonosulfate activator for sulfamethoxazole removal: performance, biotoxicity, degradation pathways and mechanism. Chem Eng J. 2018;343:676–88.
46. Lin KYA, Lin TY. Degradation of acid azo dyes using oxone activated by cobalt titanate perovskite. Water Air Soil Poll. 2018;229:10.
47. Wu LL, Lin YT, Zhang YM, Wang P, Ding MJ, Nie MH, et al. Ca $(OH)_2$-mediated activation of peroxymonosulfate for the degradation of bisphenol S. RSC Adv. 2021;11:33626–36.
48. Li ZY, Wang F, Zhang YM, Lai YX, Fang QL, Duan YX. Activation of peroxymonosulfate by $CuFe_2O_4$-$CoFe_2O_4$ composite catalyst for efficient bisphenol a degradation: synthesis, catalytic mechanism and products toxicity assessment. Chem Eng J. 2021;423:130093.
49. Kang S, Hwang J. $CoMn_2O_4$ embedded hollow activated carbon nanofibers as a novel peroxymonosulfate activator. Chem Eng J. 2021;406:127158.
50. Rastogi A, Ai-Abed SR, Dionysiou DD. Sulfate radical-based ferrous-peroxymonosulfate oxidative system for PCBs degradation in aqueous and sediment systems. Appl Catal B-Environ. 2009;85:171–9.
51. Li ZD, Sun YM, Huang WL, Xue C, Zhu Y, Wang QW, et al. Innovatively employing magnetic CuO nanosheet to activate peroxymonosulfate for the treatment of high-salinity organic wastewater. J Environ Sci-China. 2020;88:46–58.
52. Xu HD, Zhang YC, Li JJ, Hao QQ, Li X, Liu FH. Heterogeneous activation of peroxymonosulfate by a biochar-supported Co_3O_4 composite for efficient degradation of chloramphenicols. Environ Pollut. 2020;257:113610.
53. Trang NH, Kwon E, Lisak G, Hu C, Lin KYA. Cobalt ferrite nanoparticle-loaded nitrogen-doped carbon sponge as a magnetic 3D heterogeneous catalyst for monopersulfate-based oxidation of salicylic acid. Chemosphere. 2021;267:128906.
54. Khan A, Zou SH, Wang T, Ifthikar J, Jawad A, Liao ZW, et al. Facile synthesis of yolk shell Mn_2O_3@Mn_5O_8 as an effective catalyst for peroxymonosulfate activation. Phys Chem Chem Phys. 2018;20:13909–19.
55. Nguyen H, Lee J, Kwon E, Lisak G, Thanh BX, Ghanbari F, et al. Bamboo-like N-doped carbon nanotube-confined cobalt as an efficient and robust catalyst for activating monopersulfate to degrade bisphenol A. Chemosphere. 2021;279:130569.
56. Tao X, Pan PY, Huang TB, Chen L, Ji HD, Qi JJ, et al. In-situ construction of Co $(OH)_2$ nanoparticles decorated urchin-like WO_3 for highly efficient degradation of sulfachloropyridazine via peroxymonosulfate activation: intermediates and DFT calculation. Chem Eng J. 2020;395:125186.
57. Lu T, Chen FW. Multiwfn: a multifunctional wavefunction analyzer. J Comput Chem. 2012;33:580–92.
58. Zhang XL, Feng MB, Wang LS, Qu RJ, Wang ZY. Catalytic degradation of 2-phenylbenzimidazole-5-sulfonic acid by peroxymonosulfate activated with nitrogen and sulfur co-doped CNTs-COOH loaded $CuFe_2O_4$. Chem Eng J. 2017;307:95–104.
59. Al-Anazi A, Abdelraheem WH, Han C, Nadagouda MN, Sygellou L, Arfanis MK, et al. Cobalt ferrite nanoparticles with controlled composition-peroxymonosulfate mediated degradation of 2-phenylbenzimidazole-5-sulfonic acid. Appl Catal B-Environ. 2018;221:266–79.

Publisher's Note